JOURNAL OF GEOPHYSICAL RESEARCH, VOL. 106, NO. A4, PAGES 5635–5648, APRIL 1, 2001

Ion distributions in large magnetic holes in the fast solar wind

M. Neugebauer, B. E. Goldstein, D. Winterhalter, and E. J. Smith

Jet Propulsion Laboratory, California Institute of Technology, Pasadena, California

R. J. MacDowall

NASA Goddard Space Flight Center, Greenbelt, Maryland

S. P. Gary

Los Alamos National Laboratory, Los Alamos, New Mexico

Abstract. Magnetic holes are isolated localized depressions in the magnitude of the interplanetary magnetic field. Six examples of long-duration (9 to 30 min) magnetic holes observed by the Ulysses spacecraft at high heliographic latitudes near 3 AU are studied in detail. Each of the holes was in pressure balance with its surroundings. The proton-proton and alpha-proton differential streaming typically observed in the fast solar wind dropped to very low levels within the holes. The ion temperatures perpendicular to the magnetic field also increased, leading to marginal mirror-mode stability. Possible causes of these high-latitude magnetic holes are discussed. A new method of deconvolving the three-dimensional angular distributions of the protons and alpha particles from the ion instrument's angular response is described in an appendix.

1. Introduction

The term magnetic hole refers to isolated or localized depressions in the strength of the interplanetary magnetic field [*Turner et al.*, 1977]. The duration of the low-field state as a magnetic hole passes by a spacecraft is typically tens of seconds, but there is a tail to the distribution of event durations lasting up to hundreds of seconds [*Turner et al.*, 1977; *Winterhalter et al.*, 1994; *Fränz et al.*, 2000]. Magnetic holes have been observed at all heliospheric latitudes sampled by the Ulysses spacecraft, but their occurrence rate is an order of magnitude greater within 30° of the heliographic equator than it is in the high-speed polar solar wind observed during the first Ulysses orbit [*Winterhalter et al.*, 2000]. For the subset of low-latitude magnetic holes for which the field direction changed by <10°, *Winterhalter et al.* [1994] concluded that the holes were most likely relics of the mirror instability occurring upstream of the point of observation. From their analysis of magnetic holes and tangential discontinuities observed during the Ulysses fast latitude scan, *Ho et al.* [1996] also concluded that the mirror-mode instability may be the cause of magnetic holes.

The threshold condition for the mirror instability is

$$R = (\beta_\perp/\beta_\parallel)/(1 + 1/\beta_\perp) > 1, \quad (1)$$

where

$$\beta_\perp = \Sigma n_i k T_{\perp i}/(B^2/8\pi), \quad (2)$$

$$\beta_\parallel = \{\Sigma n_i k T_{\parallel i} + [\Sigma n_i m_i (v_i - v_{cm})^2/\Sigma n_i m_i]\}/(B^2/8\pi). \quad (3)$$

The summations in (2) and (3) are over all ion and electron species i with densities n_i and masses m_i. The temperatures $T_{\perp i}$ and $T_{\parallel i}$ are the second moments of the particle distributions perpendicular and parallel to the magnetic field $\boldsymbol{B}$ in a reference frame moving with the species velocity v_i. The velocity of the center of mass of the plasma is denoted by v_{cm}. The term in square brackets in the numerator of (3) accounts for any differential streaming between ion species which is not normally included in studies of the mirror instability.

Some properties of isolated decreases in magnetic field strength observed by Ulysses in the fast polar solar wind have been studied by *Tsurutani and Ho* [1999], *Tsurutani et al.* [1999], and *Fränz et al.* [2000]. *Tsurutani and Ho* [1999] and *Tsurutani et al.* [1999] question whether these high-latitude magnetic depressions have the same origin as the magnetic holes seen at low latitudes. The distributions of the depths and durations of the events are independent of latitude. At high latitudes, however, most of the magnetic depressions are bounded by sharp discontinuities, a feature that is not seen in mirror-mode structures in planetary magnetosheaths and is often absent in low-latitude magnetic holes in the solar wind. See *Tsurutani et al.* [1999] for a more complete discussion of their view that high-latitude "magnetic depressions" are not mirror-mode structures and are fundamentally different from low-latitude "magnetic holes." In this paper we use the more common term magnetic hole, without making the distinction between holes and depressions advocated by *Tsurutani et al.* [1999].

There are additional arguments against the occurrence of mirror-mode structures in the fast solar wind. The fast flow from the polar coronal holes is characterized by the presence of multiple ion beams; the alpha-particle speed exceeds the proton speed [*Neugebauer et al.*, 1996; *Feldman and Marsch*, 1997; *McComas et al.*, 2000], and there are typically two proton beams travelling at different speeds [*Feldman et al.*, 1996; *Feldman and Marsch*, 1997; *Goldstein et al.*, 2000]. In accordance with (3), this multiple beaming increases $\beta_\parallel$ such that $\beta_\perp < \beta_\parallel$, which is the opposite of the anisotropy required for the mirror instability.

Paper number 2000JA000331.
0148-0227/01/2000JA000331$09.00

If high-latitude magnetic holes are not mirror-mode structures, what are they? *Baumgärtel* [1999] has proposed a model in which magnetic holes are magnetically rarefactive MHD solitons propagating at low speeds at large angles to the magnetic field. The soliton model does not require an instability; the solitons can occur in equilibrium plasmas.

Recent work by B. Buti et al. (Generation mechanism for magnetic holes in the solar wind, submitted to *Geophysical Research Letters*, 2000) suggests another possible mechanism for the generation of magnetic holes in the solar wind. In their model and 1-dimensional simulations, magnetic holes can develop from large-amplitude right-hand-polarized Alfvénic wave packets propagating at large angles to the ambient magnetic field. The mechanism works in high-β plasmas for which the electron temperature is less than the proton temperature. The presence of anisotropies is favorable but not necessary for the generation of holes.

In this paper we use magnetic, plasma, and wave data obtained by Ulysses to study previously unexplored properties of magnetic holes in the fast polar solar wind. Because of the slow cadence of the plasma measurements, the study is necessarily limited to magnetic holes with unusually long durations. Each of the six magnetic holes we examined had qualitatively similar properties. In the final section we speculate on possible causes of these long-duration magnetic holes in the polar solar wind.

2. Instrumentation and Method of Analysis

The magnetic field data used in this analysis were obtained by the Ulysses vector helium magnetometer described by *Balogh et al.* [1992]. The instrument obtains magnetic field vectors every half second or every second, depending on the mode of operation and data rate of the spacecraft. The present analysis is based on 3-s averages of the field vectors.

We first selected the two magnetic holes on day 212 (July 31), 1994 whose field and plasma properties were previously studied by *Fränz et al.* [2000]. To obtain additional examples, we carried out an automated search for magnetic holes. The search algorithm was the same as that described by *Winterhalter et al.* [1994] with the exception that the sliding analysis window was increased from 5 min to 1 hr in order to find longer duration magnetic holes. The search covered the year 1994, when Ulysses was continuously in the high speed wind from the southern polar coronal hole as the spacecraft moved from a solar distance of 3.82 AU and a latitude of 48.4°S, to the southerly most point at 2.29 AU and 80.2°S, to 1.56 AU and 44.6°S. On the basis of the search results, we examined the magnetic field data for 2 days, 155 (June 4) and 176 (June 25), that had a large number of long-duration holes. Within those 2 days, we then (admittedly somewhat subjectively) picked out four analysis-friendly events for which good plasma spectra were available, for which the holes were discrete, isolated structures in the ambient field, and for which two consecutive holes fell within a period of four hours (to limit the data-processing effort). The properties of the selected holes are given in Table 1. The hole duration was often not well defined because many of the holes had partial recoveries and further dips before the final recovery, making the definition of the start and stop times somewhat arbitrary. Similarly, the angular change across the hole is only approximate because it depends on the choice of baseline intervals before and after the event.

The plasma data were obtained by the instrument named Solar Wind Over the Poles of the Sun (SWOOPS); the instrumentation and its performance have been described by *Bame et al.* [1992]. During each 12-s spin of the spacecraft the SWOOPS ion instrument measures ion fluxes in each of 79 angular windows for each of four energy windows. The spacing between energy windows is 5.1%. Under typical conditions, 3 or 4 spins are required to measure the proton distribution while alphas are measured during another 3 spins. Because the angle between the solar direction and the normal to the SWOOPS instrument varies greatly over the course of the Ulysses trajectory, each angular window is fairly wide (~5.5°). As the solar wind moves outward from the Sun, it cools, and the angular distribution of the spectral peaks becomes narrower. In order to determine the thermal anisotropies, it is necessary to deconvolve the angular distributions of the ions from the angular response of the instrument. The iterative method used to perform this deconvolution is described in Appendix A. A new ion spectrum is obtained every 4 or 8 min, depending on the spacecraft operational mode, which is why we selected only those holes with durations > 8 min.

SWOOPS has a separate electrostatic analyzer for measuring electrons. A three-dimensional electron spectrum was obtained every 17.3 or 34.6 min. We have linearly interpolated the electron measurements to the times of the ion spectra. At the solar distances of ~3 AU studied here, much of the distribution of core electrons is hidden under the spacecraft photoelectron peak and the calculated electron density is lower than the true density. For the analysis that follows, we use $T_{\perp e}$ and $T_{\parallel e}$ determined from the part of the distribution not affected by photoelectrons, but calculate the electron density n_e to give charge neutrality; $n_e = n_p + 2\,n_\alpha$.

The Unified Radio and Plasma wave (URAP) investigation uses an electric field antenna system consisting

Table 1. Summary of magnetic holes included in study.

Year/ Day	UT[a]	Duration, min	R, AU	Latitude, deg	Angular Change, deg	Entry Boundary[b]	Exit Boundary[b]	Langmuir Waves?	Ion Acoustic Waves?	Whistlers?
94/155	1646-1656	10	3.0	-66.6	128	?	TD	yes	yes	yes
	1715-1724	9			51	TD	TD			
	1646-1724	38			83	?	TD			
94/155	1831-1844	13	3.0	-66.6	55	TD	ND	no	no	yes?
94/176	0824-0854	30	2.9	-69.8	86	TD	RD	?	no	no
94/176	0914-0936	22	2.9	-69.8	98	?	TD	yes	yes	no
94/212	0440-0500	20	2.8	-75.5	81	TD	TD	yes	?	?
94/212	0638-0647	9	2.8	-75.5	38	TD	TD	no	no	no
	0638-0654	16			23	TD	TD			

[a] More than one time interval is given when there is more than one reasonable choice of hole boundaries.

[b] TD, tangential discontinuity; RD, rotational discontinuity; question mark, normal direction not well determined; ND, a discontinuity (perhaps a slow-mode shock?) with both a large magnitude change and a normal component of **B**.

of a 7.5-m monopole antenna along the spacecraft spin axis and a 72.5-m tip-to-tip dipole antenna in the spacecraft spin plane. These antenna are connected to several receivers [*Stone et al.,* 1992] covering the frequency range from 0.1 Hz to 940 kHz. The receivers detect a variety of wave modes, including Langmuir mode at the electron plasma frequency f_{pe} and ion acoustic mode at a fraction of f_{pe}. In addition, dual search coils permit detection of magnetic waves in the frequency range from 0.2 to 450 Hz, corresponding to whistler mode frequencies. Such waves are frequently found to occur in magnetic holes [*Lin et al.,* 1995].

3. Observations of Several Long-Duration Magnetic Holes

Figure 1 shows 3-s averages of the magnitude and the components of the heliospheric magnetic field for a 4-hour interval on day 176 (June 25), 1994. The standard heliospheric RTN (Radial, Tangential, Normal) coordinate system is used. During that interval there were two long-duration magnetic holes, one from 0824 to 0854 UT and another from 0914 to 0936 UT. There were also several holes too brief for plasma data analysis. Both of the long-duration holes were bounded by discontinuities. A principal-axis analysis [*Sonnerup and Cahill*, 1967; *Smith*, 1973; *Lepping and Behannon*, 1980] of these four discontinuities suggests that the first (at 0824 UT) and the last (at 0936 UT) were tangential discontinuities, the second at (0854 UT) was probably a rotational discontinuity, while the normal to the third (at 0914 UT) could not be determined because the directional change was largely confined to a line rather than tracing out a planar arc. A significant difference between this pair of holes and the holes studied by *Winterhalter et al.* [1994, 2000] is that the field rotated through large angles across both the long-duration holes (see Table 1). Neither of these holes could be called a "linear hole" for which the field direction changes by only a few degrees.

Figure 2 displays the variations of some of the plasma parameters during the interval shown in Figure 1. Figure 2a repeats the field magnitude shown in Figure 1. Figure 2b shows the proton temperatures perpendicular and parallel to the magnetic field calculated by the iterative technique described in the appendix. At times, $T_\perp$ exceeded $T_\parallel$ within the holes; everywhere else, $T_\parallel > T_\perp$, as is typical of the

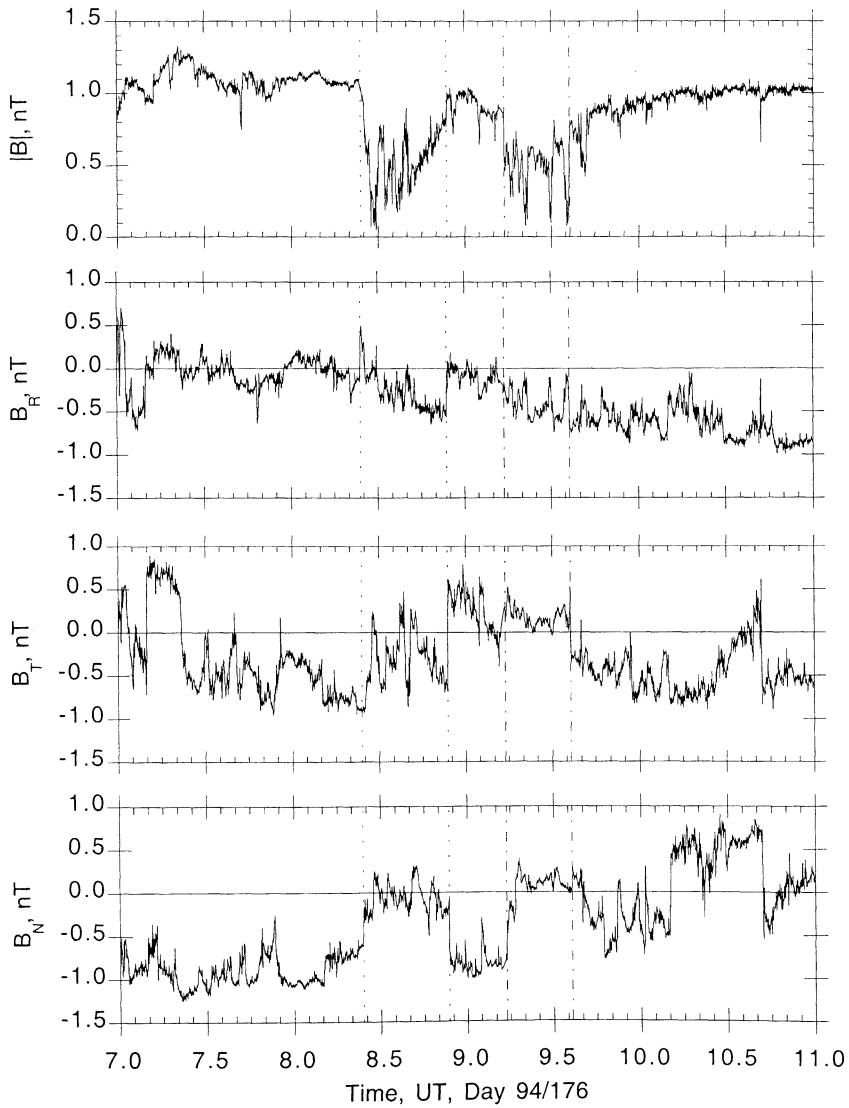

Figure 1. Magnetic field measurements for 0700-1100 UT on day 176 (June 25), 1994. From top to bottom are the field magnitude and the radial, tangential, and normal components. The time resolution is 3 s. Vertical dashed and dash-dot lines indicate the magnetic hole boundaries.

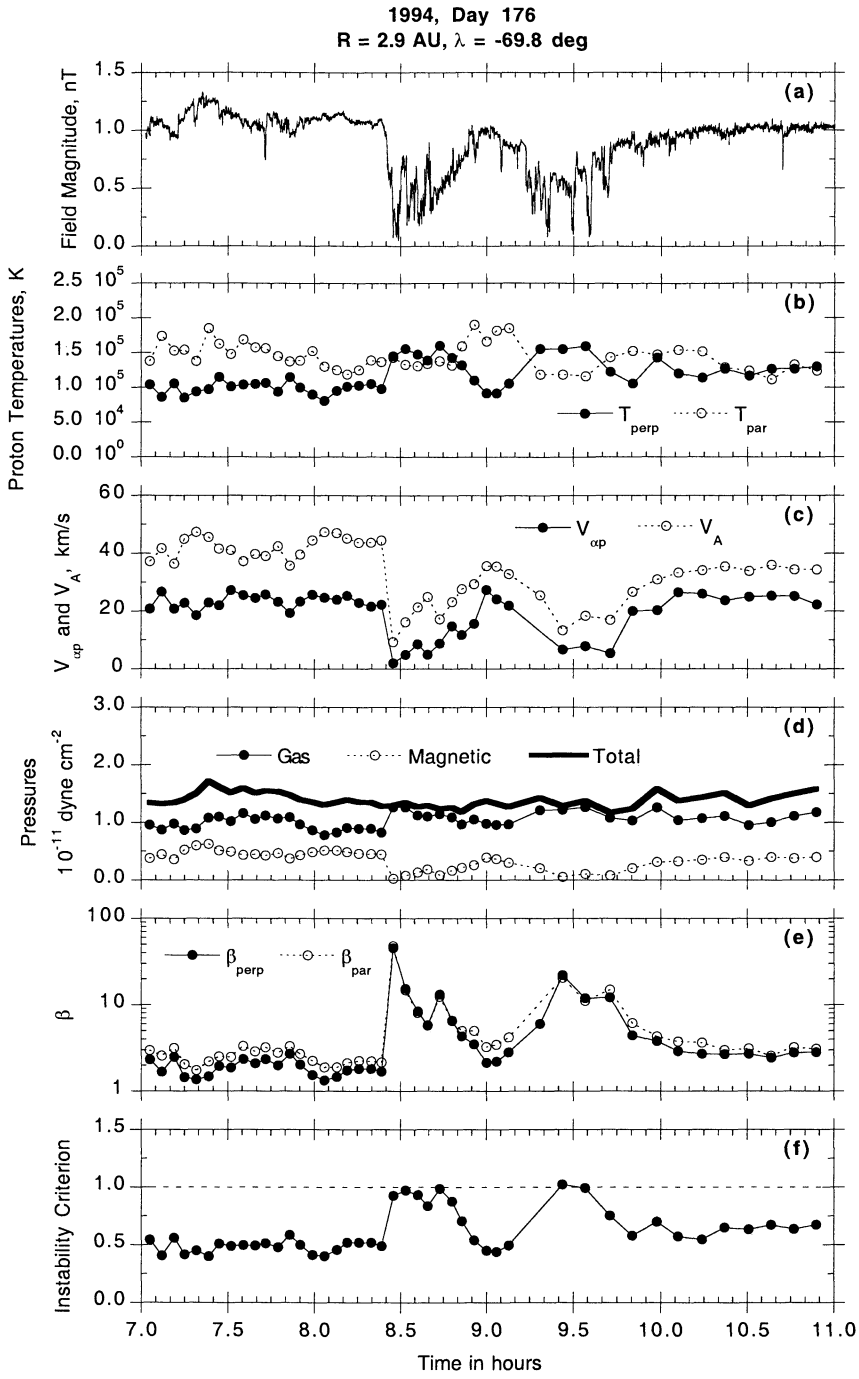

Figure 2. Selected parameters for the interval 0700-1100 UT on day 176, 1994. (a) magnitude of the magnetic field; the same as in Figure 1(top). (b) The proton temperature measured parallel to (open circles) and perpendicular to (solid circles) the magnetic field. (c) The Alfvén speed (open circles) and the magnitude of the vector differential flow between protons and alpha particles (solid circles). (d) Pressures, with the magnetic pressure indicated by open circles, the plasma pressure by solid circles, and their sum by the thick solid line. (e) The values of $\beta_{\|}$ (open circles) and $\beta_{\perp}$ as defined by (2) and (3). (f) The mirror-mode instability criterion as defined by (1).

fast solar wind. This variation is consistent with the finding of *Fränz et al.* [2000] that the ratio of $T_{\perp}/T_{\|}$ for protons is generally higher inside magnetic holes than in the ambient solar wind observed by Ulysses. The ~50% changes in $T_{\perp}$ between the ambient solar wind and the magnetic holes exceed the expected measurement errors. A systematic uncertainty derives from the ~10% uncertainty in the calibration of the particle detectors (D. J. McComas, personal communication, 2000), but the same detectors recorded counts both within and outside the holes, so relative changes in temperature would not be strongly affected. The deconvolution algorithm described in the appendix accepts a solution if $T_{\|}$ and $T_{\perp}$ change by <5% between the second and third iterations. For most spectra the calculated temperatures changed by much less than this upper limit of 5% between iterations.

Additional information can be obtained from the

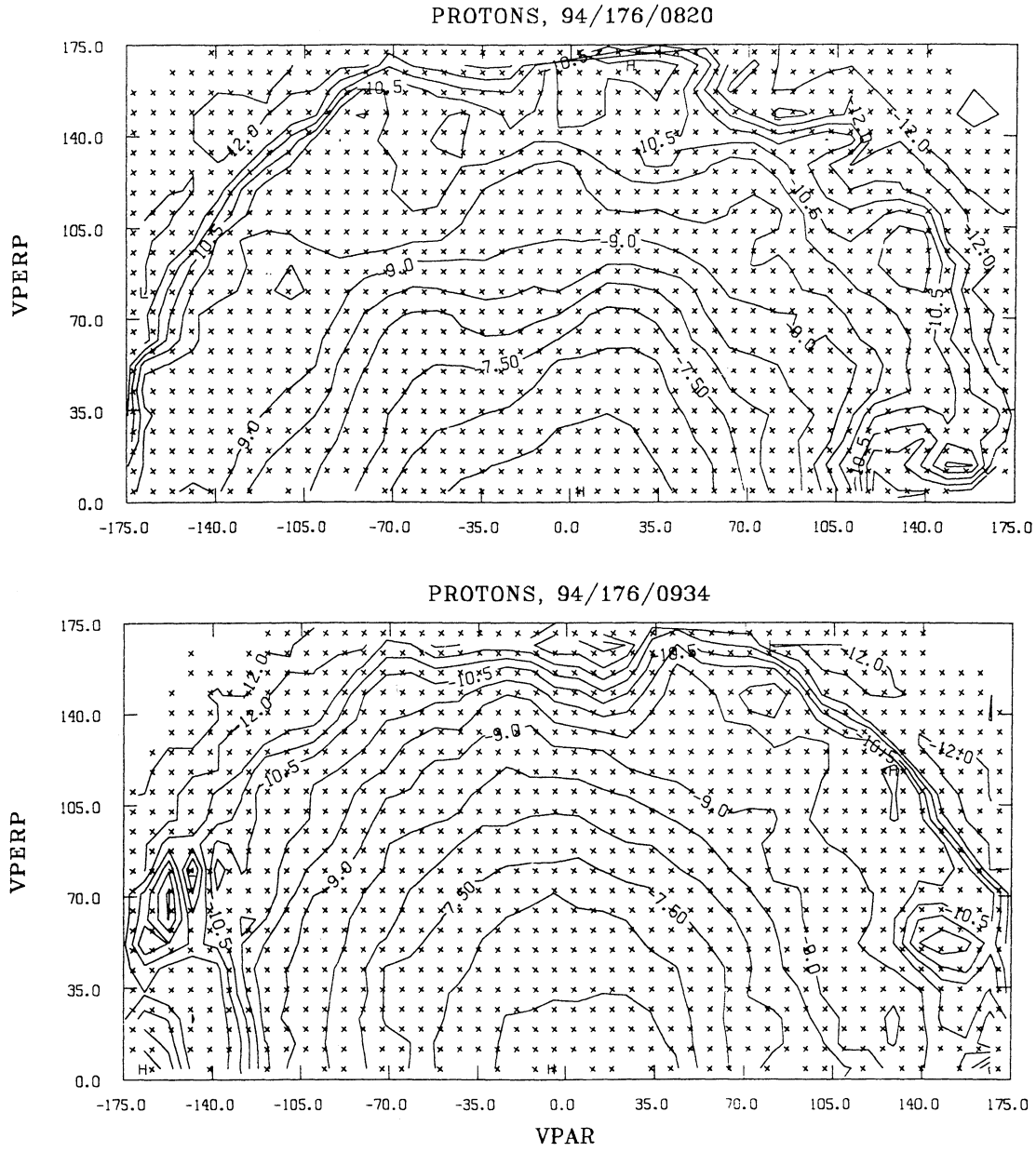

Figure 3. Proton distribution functions in $v_{\|}$-$v_{\perp}$ coordinates for two selected spectra (top) adjacent to and (bottom) within a magnetic hole. There are two contours per decade in $f(v)$ and the crosses mark the bins in which there are data.

contour diagrams of the proton distribution functions shown in Figure 3. The contours are plotted at half-decade intervals and the crosses denote bins in $v_{\|}$-$v_{\perp}$ space for which there were data. The top distribution was obtained at 0820 UT, just prior to the encounter with the first magnetic hole. It shows a typical two-stream proton distribution function observed in the high-speed solar wind. Because the observations were obtained in the southern hemisphere where the heliospheric field was inward toward the Sun, the faster stream is to the left of the origin. The density of the faster stream was less than the density of the slower stream (to the right of the origin), again as is typical. The velocity distribution of the protons observed at 0934 UT within the second magnetic hole is shown in Figure 3(bottom). It differs greatly from the distribution in the ambient plasma. The distribution appears to be close to a bi-Maxwellian with $T_{\perp} > T_{\|}$.

Figure 2c shows time sequences of the Alfvén speed V_A and the magnitude of the differential flow velocity vector V_{ap} between the protons and alpha particles. In all cases V_{ap} was less than V_A, which is typical for solar distances greater than 1 AU [*Neugebauer et al.*, 1996]. Both V_{ap} and V_A decreased to very low values within the magnetic holes, with the differential flow between protons and alpha particles nearly disappearing.

Figure 4 shows contours of the alpha-particle distribution functions both outside of (top) and within (bottom) the magnetic hole. Outside the hole the alpha-particle temperature parallel to the field greatly exceeded the perpendicular temperature, with hints of multiple alpha-particle streams. Inside the hole the anisotropy was reversed, with $T_{\perp} > T_{\|}$ for the alphas as well as for the protons.

The bottom three plots in Figure 2 show plasma parameters taking account of all three species, protons, alphas, and electrons. Two electron spectra were obtained during the passage of the first magnetic hole. For both of those spectra, $T_{\perp}$ and $T_{\|}$ were both lower and $T_{\perp}/T_{\|}$ was higher within the hole

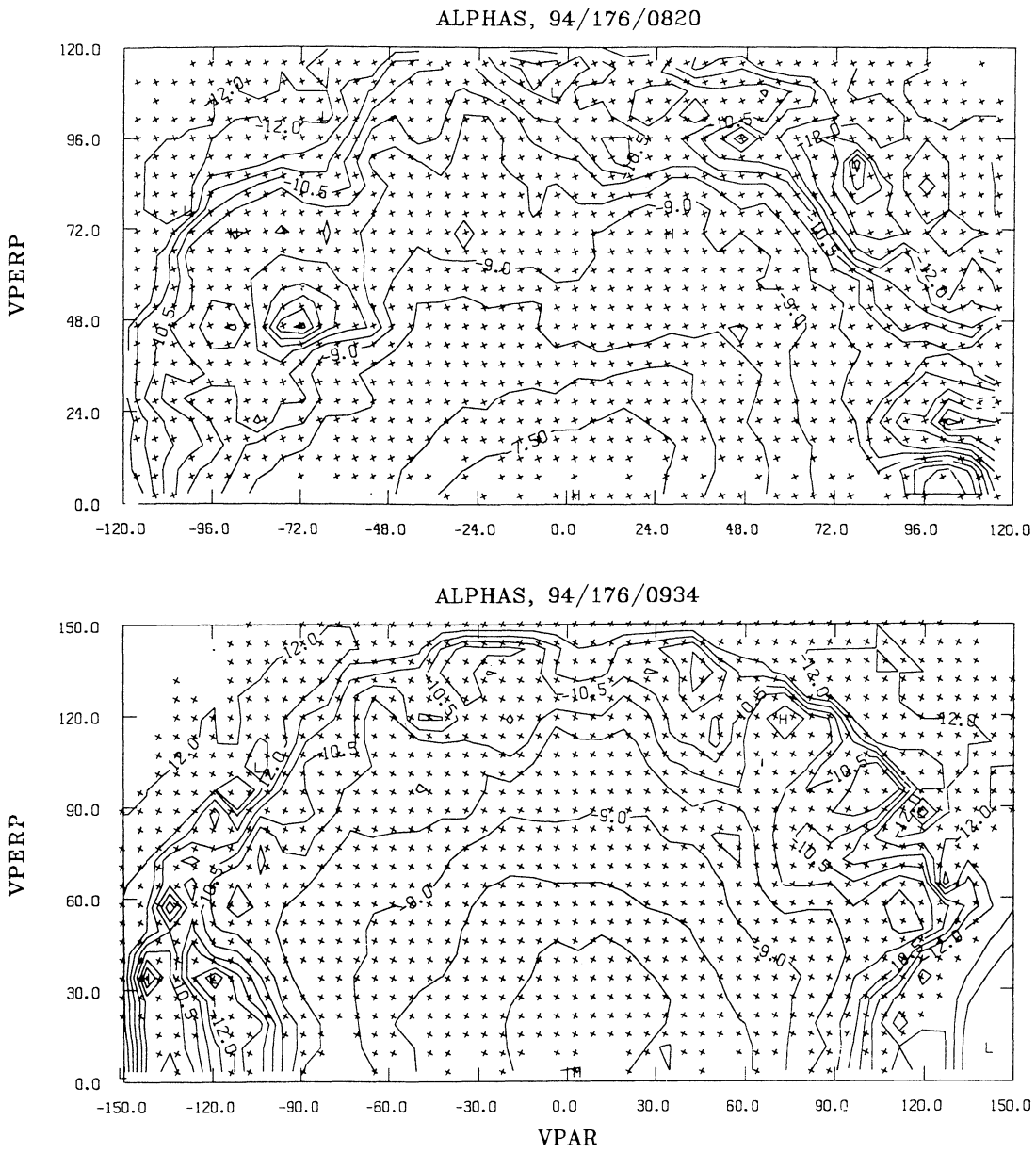

Figure 4. Same as Figure 3, but for alpha particles rather than for protons.

than outside it. No electron spectrum was obtained within the second hole. Figure 2d shows the pressures of the gas (ΣnkT, where $T = T_{\|}/3 + 2\ T_{\perp}/3$ and the sum is over protons, alphas, and electrons), of the magnetic field ($B^2/8\pi$), and of their sum. The gas pressure increased slightly inside the holes while the total pressure remained approximately constant. In other words, the holes were pressure balance structures.

Figure 2e is a plot of $\beta_{\perp}$ and $\beta_{\|}$, taking the anisotropies of the protons, alphas, and electrons and the differential streaming between species into account according to (2) and (3). The scale is logarithmic. Except in the holes, $\beta_{\|}$ is greater than $\beta_{\perp}$. Both components of β are unusually high inside the holes.

Finally, the mirror-mode instability criterion R defined in (1) is plotted in Figure 2f. R averaged 0.4 to 0.7 outside the holes and approximately equaled the instability threshold (indicated by the dashed line) inside the magnetic holes.

Figures 5 and 6 show data for two other 4-hour intervals with magnetic holes similar to those observed on day 176 of 1994. The formats are the same as that of Figure 2. These holes passed the Ulysses spacecraft on day 155 (June 4) and day 212 (July 31) of 1994. The rotations of the field direction across the four holes shown in Figures 5 and 6 are listed in Table 1; all the rotations were large compared to linear holes. Principal-axis analyses of the 3-s plots of the field components revealed that each of the four holes was bounded by discontinuities whose identifications as tangential or rotational are also given in Table 1. Electron spectra were available in the first hole on day 155 and in both holes on day 212. In each case, the electron $T_{\|}$ dropped while $T_{\perp}/T_{\|}$ increased within the holes. The changes in $T_{\perp}$ were smaller and within the range of fluctuations in the ambient wind.

On the basis of Figures 2, 5, and 6 we conclude that the plasma and field variations across all six of the holes included in this study were remarkably similar. There were greater hole-to-hole differences in the structure of plasma waves within the six holes, however. Figures 1, 2, 5, and 6 demonstrate that each of the holes showed fluctuations in

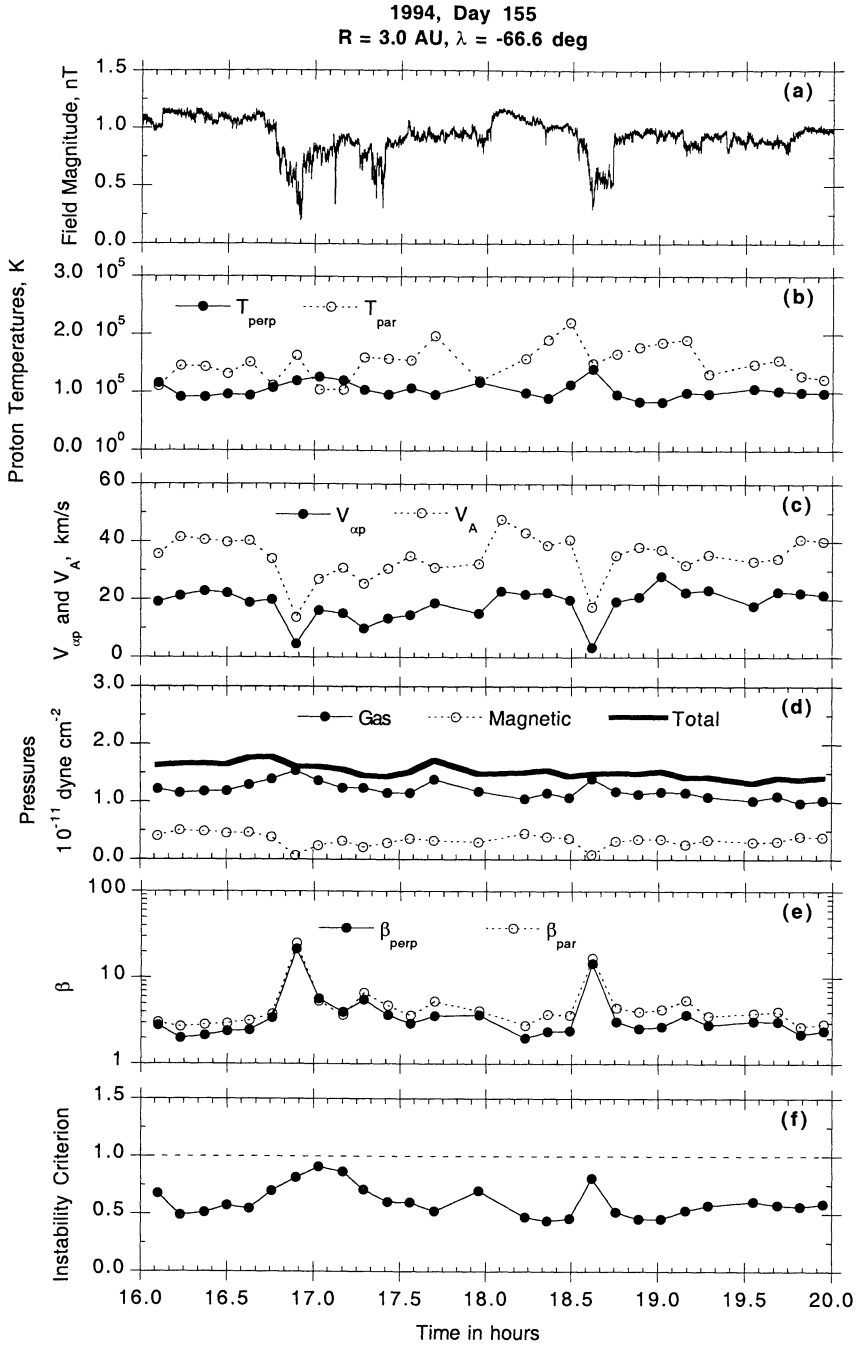

Figure 5. Same as Figure 2 for the interval 1600-2000 UT on day 155 (June 4), 1994.

both the magnitude and direction of the field with periods of a few minutes, but the magnetic field in some holes was noisier than in others. URAP plasma-wave data were inspected for the presence or absence of Langmuir waves, ion acoustic waves, and whistlers. Table 1 includes a summary of which plasma waves were detected in each of the six magnetic holes. The results are mixed; no wave mode was present in all the holes and some holes appeared to have no detectable plasma waves within the URAP frequency range. There was not a strong correlation between the presence or absence of waves and the value of the mirror-mode instability ratio R.

4. Discussion

In the previous section we displayed some properties of six long-duration magnetic holes observed by Ulysses at high latitudes in the fast solar wind. Magnetically, all six were bounded by discontinuities, most of which were tangential discontinuities. Several previous studies have revealed the frequent occurrence of directional discontinuities at the boundaries of magnetic holes [*Lin et al.*, 1995; *Ho et al.*, 1996; *Lin et al.*, 1996; *Tsurutani et al.*, 1999]. Of the 115 high-latitude magnetic holes analyzed by *Fränz et al.* [2000], 78% were bounded by discontinuities. Analysis of 129 such boundary discontinuities by *Tsurutani et al.* [1999] showed that 61% of them were tangential discontinuities. At least in this respect, the long-duration holes that were the object of this study were consistent with previous studies of high-latitude magnetic holes.

The holes had complex structures within those boundaries. Most of them appeared to have several deep, narrow holes within the overall structure of the hole. Such

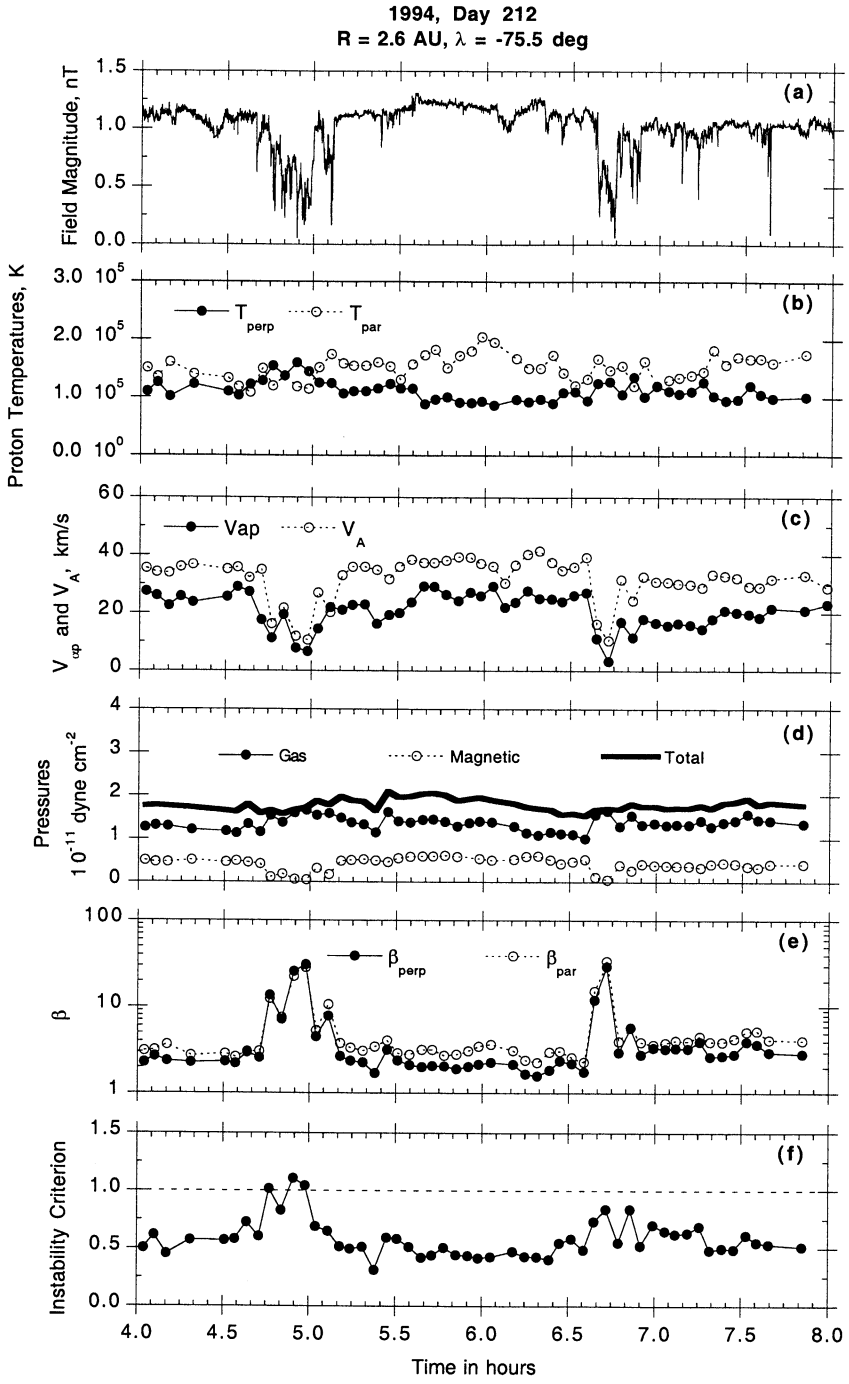

Figure 6. Same as Figure 2 for the interval 0400-0800 UT on day 212 (July 31), 1994.

fine structure is consistent with the interpretation of two long-duration holes observed upstream of the Earth's bow shock as being conglomerations of individual magnetic holes into a larger structure [*Chisham et al.*, 2000].

The plasma properties of the six holes were remarkably similar. This result does not necessarily follow from the selection of the holes for study because the plasma data (and the wave data) were not examined until after the sample holes had been chosen on the basis of their magnetic signatures (duration, depth, and relative isolation from other structures) alone. The plasma data revealed the following common features of the magnetic holes included in this study: (1) The decreased field strength was accompanied by increased density (and in some cases increased temperature) such that the magnetic holes were in pressure balance with their surroundings. (2) The combination of decreased field strength and increased density resulted in low values of the Alfvén speed and high values of the plasma β. (3) The differential streaming between the alphas and the protons and between the two proton beams decreased, almost to the point of disappearance. (4) The proton and alpha particle temperatures perpendicular to the magnetic field increased above their ambient values. (5) The combination of loss of differential streaming and increased perpendicular temperatures led to the increased values of the anisotropy $T_\perp/T_\parallel$ for both protons and alpha particles. *Fränz et al.* [2000]

had previously noted the increase in $T_\perp/T_\parallel$ for protons in magnetic holes. (6) When electron data could be obtained within the holes, they indicated a decrease in $T_\parallel$ and an increase in $T_\perp/T_\parallel$ compared to electrons in the ambient solar wind. (7) The increased β together with the increased anisotropy corresponded to a state of marginal mirror-mode stability, in contrast to the apparently very stable state of the ambient plasma.

How can these observations be explained? What caused these magnetic holes? We consider first a multistep scenario. The assumed initial condition is the existence of a large directional discontinuity in the interplanetary magnetic field. In many such discontinuities the magnitude of the magnetic field decreases significantly in the middle of the discontinuity as the field changes direction [e.g., *Burlaga*, 1968; *Neugebauer et al.*, 1984]. An example can be seen at 1042 UT in Figure 1. In the region of decreased field strength, the Alfvén speed V_A is also lower than in the ambient plasma. If V_A is low enough, the differential streaming velocities $V_{\alpha p}$ and V_{pp} become unstable. Simulations by *Gary et al.* [2000] show that wave-particle scattering by electromagnetic fluctuations from alpha-proton instabilities can reduce the alpha-proton relative streaming, heat the alphas, and increase $T_\perp/T_\parallel$ for the alphas. Similarly, instability of proton-proton streaming results in increased $T_\perp$ for protons [*Daughton et al.*, 1999]. The magnetosonic and Alfvén waves responsible for scattering the protons or alphas out of the streaming beam have frequencies within the range of the Ulysses magnetometer. Figures 1, 5, and 6 show considerably enhanced fluctuations of the field magnitude within the holes, which could be signatures of either magnetosonic waves or large-amplitude, nonlinear Alfvén waves. Figure 1 doesn't show large increases in the fluctuations of the field components for the magnetic holes observed on day 176, but the fluctuations in the field components did increase in the four other holes studied; thus both magnetosonic and Alfvén waves were probably excited. The cadence of the plasma measurements was too slow to allow detailed studies of these waves.

Once the differential streaming has been reduced and the anisotropy has been increased, the plasma is subject to either the ion cyclotron or the mirror-mode instability [*McKean et al.*, 1994]. The average field strength within the magnetic holes was approximately 0.25 nT, which corresponds to a proton thermal gyroradius of ~150 km. Structures of that size excited by ion cyclotron waves would be carried past the spacecraft in 0.2 s, yielding a Doppler-shifted frequency of 5 Hz. There is a small gap in the frequency coverage of the URAP search-coil detectors from 5 to 9 Hz because the low- and high-frequency band receivers do not overlap. Although this gap complicates the detection of possible ion cyclotron waves, the search-coil data do not support the existence of those waves in magnetic holes. This generally negative result for ion cyclotron waves is consistent with theoretical expectations that for the high β and appreciable alpha-particle densities in the solar wind considered here, the ion cyclotron instability is less likely to arise than is the mirror-mode instability [*Gary et al.*, 1993]. The mirror instability may allow the magnetic hole to grow until the observed state of marginal stability is reached. Because the plasma was not strongly mirror-mode unstable at the points of observation, if the mirror-mode instability was involved in the creation of these structures, it must have operated somewhere upstream.

We acknowledge that it is highly unorthodox to think of a parallel-velocity driven instability (e.g., a two-beam instability) leading to a perpendicular-velocity driven instability (e.g., a mirror-mode instability). But what we may have is a series of events, each of which feeds the next under a set of unusual circumstances. If there were no differential streaming in the plasma, the plasma in the region of depressed field strength in the middle of the discontinuity would be stable, but the decrease of the Alfvén speed in the low-field region destabilizes the preexisting differential streaming. The end point of the proton-proton and alpha-proton instabilities would also be a stable configuration were it not for the circumstance that the plasma β within the discontinuity is so unusually high that the plasma is then unstable to the mirror mode.

The observation of various plasma wave modes suggests that several electron instabilities are also likely to be operating in the regions of these magnetic holes. Some of our holes contained Langmuir, ion acoustic, and/or whistler waves, while others did not. This result is consistent with previous findings by *Lin et al.* [1995, 1996]. Most of the Langmuir wave bursts observed by Ulysses at high southern latitudes in 1994 were associated with magnetic holes [*Lin et al.*, 1995]. *MacDowall et al.* [1996] have suggested that the waves are generated as a result of the unstable electron beam formed by the conservation of the magnetic moment of electrons flowing into the low-field region. We cannot test this suggestion directly because most of the magnetic holes are bounded by tangential discontinuities so we cannot follow events along a streamline. The electron temperatures and anisotropies within the holes suggest, however, that some instability has operated upstream of the point of observation to destroy the conservation of the electron magnetic moment.

Before leaving consideration of the mirror mode, we address the question of whether or not the value of R calculated outside the holes is correct. Its calculation was based on only those ions and electrons that could be measured by the SWOOPS instrument. Is it possible that pickup ions or energetic particles could provide enough additional anisotropy to raise R to a value close to unity? If it is assumed that the pickup ion population is so anisotropic that its $T_\parallel = 0$ (an unrealistic, extreme assumption) and its $T_\perp$ corresponds to a thermal speed equal to the solar wind speed of ~750 km/s, then a density of $\sim 1.5\times10^{-3}$ cm^{-3} H^+ or 0.4×10^{-3} cm^{-3} He^+ pickup ions could raise the total $\beta_\perp$ sufficiently to yield $R = 1$. Integration of the pickup-ion phase-space density spectra, such as those shown in Figures 2 and 4 of *Gloeckler and Geiss* [1998], yield estimates of pickup ion densities near 3 AU of 1.25×10^{-4} cm^{-3} for H^+ and 8.5×10^{-5} cm^{-3} for He^+ (G. Gloeckler, personal communication, August, 2000). We conclude that it is not possible for pickup ions to raise the ambient plasma to the mirror-mode instability threshold unless the pickup ion densities and anisotropies at the times we studied were very much greater than the average values near 3 AU. This conclusion agrees with that of the study of magnetic holes observed during the Ulysses fast latitude scan [*Winterhalter et al.*, 2000]. Any energetic electrons or ions from the Sun are more likely to be streaming along the field with $T_\parallel >> T_\perp$ so they are also not expected to raise the value of R.

There are perhaps other causes of the magnetic holes that do not involve the mirror-mode instability. *Baumgärtel* [1999] has suggested that magnetic holes can result from MHD soliton solutions of the Derivative Nonlinear Schrödinger equation. We think the soliton model does not provide a good fit for the long-duration magnetic holes studied here. First, if the holes had been caused by the passage of a soliton, the magnetic field after the hole would have returned to its initial direction, which is not the case for the holes in this study. There is also a question of whether or not the destruction of the differential streaming could proceed within the time it would take a soliton to propagate through the region; *Reisenfeld et al.* [2000] estimate an alpha-proton relaxation time of the order of 10^5 s. Finally, the major

tangential discontinuities at the boundaries of and within the holes are not a feature of the soliton model. Our conclusion concerning the poor fit to a soliton model agrees with the similar conclusion reached by *Tsurutani et al.* [1999].

The generation of magnetic holes by the propagation of large-amplitude Alfvénic wave packets at large angles to the magnetic field, as studied by Buti et al. (B. Buti, personal communication, paper in preparation, 2000) is perhaps a possibility. In a recent simulation, Buti followed the evolution of large amplitude right-hand polarized Alfvénic wave packets propagating at 80° to the field direction in a high-β plasma whose properties closely matched those studied here. Specifically, the parameters were $T_\perp/T_\parallel = 0.8$ for both protons and alphas, $T_\alpha = 4T_p$, $T_p = 3T_e$, and $V_{\alpha p} = 0.5V_A$. The wave packets were found to evolve into linear (i.e., little rotation of the field direction) magnetic holes. The alpha particles were preferentially heated. The holes with differential streaming ($V_{\alpha p} \neq 0$) were narrower and not as deep as in the case of $V_{\alpha p} = 0$. This work is continuing and will be reported shortly.

An issue with each of these proposed sources of magnetic holes is the hole dimensions. The mirror instability is a kinetic phenomenon which grows at relatively short wavelengths of tens of proton gyroradii or thousands of km [*Tsurutani et al.*, 1992]. The transverse Alfvén wave mechanism leads to similar size holes. The thickness of Baumgärtel's soliton-generated holes ranges from 8 to 60 times the proton inertial length, or 3000 to 25,000 km. The thickness of the holes we studied was on the order of 10^6 km. A possible scenario has been offered by *Chisham et al.* [2000] wherein large holes are formed from a conglomeration or coalescence of successive smaller magnetic minima. The time profiles of field magnitude shown in Figures 1, 5, and 6 support such a model.

A final question is whether the magnetic holes might be remnants of solar structures. The presence of tangential discontinuities at most of the boundaries of the magnetic holes agree with a scenario in which the solar wind flux tubes threading the holes might always have had lower fields than their neighbors, with a consequent limitation of the differential streaming allowed along them. The cases of rotational-discontinuity boundaries are not consistent with such a scenario, however. A difference in the chemical composition of the solar wind inside the holes than outside would be indicative of a solar origin. We searched for and could not find any significant variations of the alpha-particle abundances in the holes, however. In a study of large-scale magnetic holes observed near Earth with the ACE spacecraft, *Zurbuchen et al.* [2000] found no significant differences in the elemental abundance ratio of Fe to O or in the charge state ratio O^{7+}/O^{6+} in magnetic holes compared to the surrounding solar wind. Their findings are consistent with the magnetic holes forming above the region of the solar corona where the charge state is frozen into the plasma. Zurbuchen et al. suggest that magnetic holes may be created by reconnection of oppositely directed loops of plasma above the critical point where the wind becomes supersonic. The applicability of such a model to the high-latitude solar wind flow from coronal holes with unipolar fields rather than large loops is questionable.

In summary, we cannot prove what caused these long-duration magnetic holes in the fast, high-latitude solar wind, but a series of events that left the plasma in a state of marginal mirror-mode stability may be a possibility. More theoretical work that includes multiple ion beams would be welcome.

Appendix A: Deconvolution of the Angular Data

The Ulysses SWOOPS ion spectrometer measures particle counts in three-dimensional windows defined by energy/charge and two angles. The fields of view of both the polar and the azimuthal angles in the rotating spacecraft coordinate system are roughly 5.5°×5.5°; see *Bame et al.* [1992] for greater detail. In the high-speed polar solar wind where the speed is ~750 km/s, each angular window corresponds to a dimension in velocity space of ~ 65×65 km/s. This window size exceeds the ~40 km/s thermal speed in the fast wind at ~2 AU near the solar poles. The thermal speed is even lower than that at greater solar distances along the Ulysses trajectory. The SWOOPS energy resolution ($\Delta E/E \approx 0.05$) allows good estimates of the thermal distribution in the radial direction, but the wide angular resolution prevents determination of the thermal anisotropy unless the angular distribution of the plasma can be corrected for or separated from the angular response of the instrument.

One method of accomplishing such a deconvolution is to carry out a least-squares fit to an assumed distribution function such as a bi-Maxwellian. There are two major problems with using the least squares technique. First, the fitting algorithm sometimes homes in on a local minimum that is not the best possible fit to the data. Second, we wish to determine actual distribution functions that may not resemble a bi-Maxwellian or any other simple function. This appendix briefly summarizes our deconvolution method.

The process starts conventionally with the definition of phase space density given by

$$f(u, \theta, \varphi) = C/u^4 G, \tag{A1}$$

where C is the number of counts accumulated in a three-dimensional window in velocity space, $\boldsymbol{u}$ is velocity in the spacecraft frame of reference and coordinates, and G is a geometric factor which includes the instrument aperture area and counting efficiency, the time over which counts are accumulated, and the transmission function of the field of view. Fluid parameters are calculated from the moments of the distribution over all velocity space. Accordingly, the particle number density is given by

$$n = \int f(u, \theta, \varphi)\, d^3u, \tag{A2}$$

where d^3u is the volume element in velocity space

$$d^3u = u^2\, du\, \sin\theta\, d\theta\, d\varphi. \tag{A3}$$

Higher moments, such as the x component of velocity u_x, can then be computed as

$$\langle u_x \rangle = \int u \sin\theta \cos\varphi\, f(u, \theta, \varphi)\, d^3u / n. \tag{A4}$$

In practice, moments are calculated by summing over all the 3-D windows in velocity space as

$$\langle u_x \rangle = \Sigma C_i \int (u_x/Gu^4)\, d^3u/n \tag{A5}$$

where a table of integrals (or algebraic algorithms) is compiled for each 3-D window for each function whose moment is to be computed. Note that in calculating the integrals in (A5), the function G is not a constant. For the Ulysses instrument it is approximated by a trapezoid in θ and a rotationally smeared Gaussian in φ [*Bame et al.*, 1992].

In step 1, the deconvolution begins by subtracting the bulk velocity vector calculated from (A5) and similar equations for u_y and u_z from the velocity space address of each 3-D window (or pixel) to yield 3-D addresses (v_x, v_y, v_z) in a coordinate system moving with the plasma.

In step 2a, it is assumed that the ion distribution is gyrotropic. The measured direction of the magnetic field is used to rotate the data into a magnetic coordinate system by calculating a 2-D velocity vector ($v_\parallel$, $v_\perp$) for the 3-D position (v_x, v_y, v_z) of each pixel in velocity space. The 2-D velocity space is then broken into equal-sized bins. Note that "pixels" (and subpixels) refer to windows in instrument coordinates, while "bins" refer to two-dimensional $v_\parallel$-$v_\perp$ sections of velocity space. The dimensions and spacings of the bins are (0.1 w + 2) km/s where w is the thermal speed calculated from the second moment of the original distribution function. With bins of that size, a matrix with 50 values of $v_\parallel$ by 25 values of $v_\perp$ adequately covers the distribution from its peak to the background noise level. An average value of $<f(v)>$ is calculated for each bin in $v_\parallel$-$v_\perp$ space. Some of the $v_\parallel$-$v_\perp$ bins far from the origin can have values of $<f(v)> \leq 0$ as a result of the subtraction of an average background from the counts in each pixel. The value of $<f(v)>$ for those bins is set to a small positive value such as 10^{-12} $s^3km^{-3}cm^{-3}$.

In step 2b, contours of constant values of $z = \log_{10}<f(v)>$ are calculated from the matrix generated in step 2a after it has been reflected about the abscissa. The contouring technique uses the method of natural neighbor interpolation as implemented in the nngridr program (D. Watson, nngridr: An implementation of natural neighbor interpolation, 1994, available from P.O. Box 734, Claremont, WA 6010 Australia) distributed as part of the NCAR graphics package. An example of the resulting proton contours is shown in Figure A1. Contour lines are drawn at half decade levels of $< f(v)>$, and the plus signs indicate bins with measurements in them.

The need for deconvolution can be understood by comparing the spacing of the contours in Figure A1 with the ~65×65 km/s size of the angular windows. There are often changes in $<f(v)>$ of more than 2 orders of magnitude from one side of a pixel to the other.

In step 3a, each 3-D pixel is divided into 64 subpixels with 1 energy/charge by 8 azimuthal by 8 polar angle subpixels. Values of u_{xi}, u_{yi}, u_{zi}, d^3u_i , and τ_i are calculated for each of the i = 1 to 64 subpixels. The bulk speed calculated from (A4) and used in step 1 is used to transform the velocities from the instrument to the plasma reference frame. τ_i is the average transmission function (or the fraction of an incident beam that can pass through the analyzer to the detector) of a subpixel; it is unity for a subpixel at the center of a pixel and approaches zero for subpixels near the edges of a pixel.

In step 3b, the counts C in each pixel are then distributed among its 64 subpixels. This is accomplished by (1) finding the values of $v_{\parallel i}$, $v_{\perp i}$ corresponding to the velocity address (v_{xi}, v_{yi}, v_{zi}) of each subpixel; (2) finding $f_i^* = f(v_{\parallel i}, v_{\perp i})$ by interpolation from the contours (the asterisk denotes a parameter calculated from the contours rather than from the data); and (3) calculating the counts C_i in subpixel i from

$$C_i = C f_i^* \tau_i / \Sigma(f_i^* \tau_i) \quad \text{(A6)}$$

where the summation is over all the subpixels in a pixel.

In step 4, subpixel values of f_i are then calculated from the subpixel C_i

$$f_i = C_i (\Sigma \tau_i)/ \tau_i G u^4 \quad \text{(A7)}$$

In general, the individual values of f_i do not equal the values f_i^* derived from the contours.

In step 5a, bin averages of f_i in $v_\parallel$-$v_\perp$ space are then computed from all the values of f_i from all the subpixels of all the pixels. Because the number of "measurements" is now 64 times greater than in the original matrix, there are many fewer empty bins and more values are included in each bin.

In step 5b, the new values of $<f(v)>$ are used to compute new contours, following the methods in step 2b.

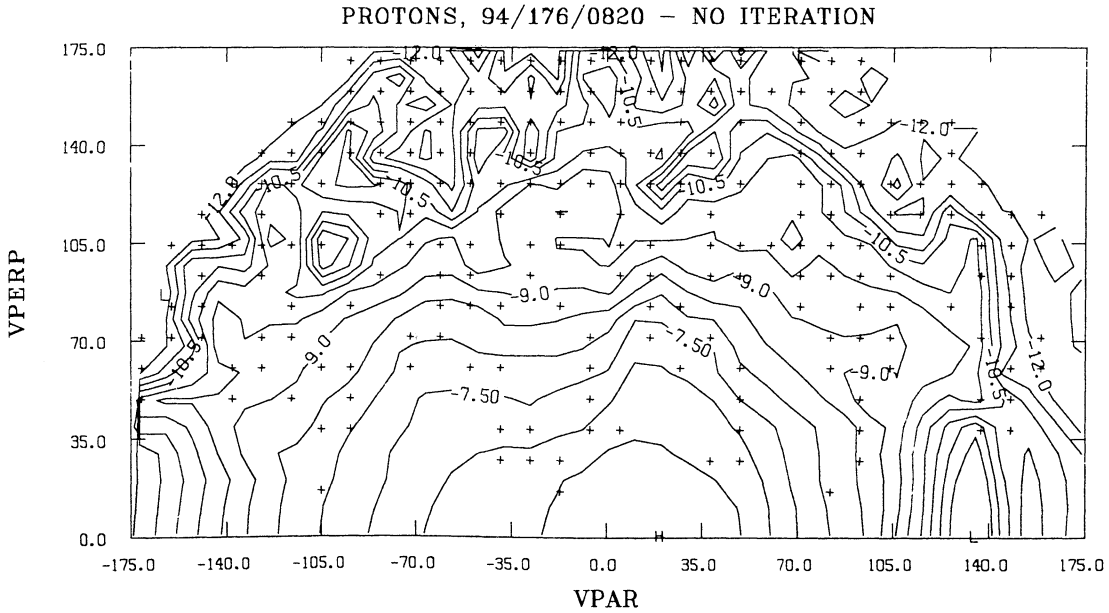

Figure A1. Proton distribution function for the same spectrum as that shown in Figure 3(top), but based on only the full pixel, rather than subpixel, data, before any iteration was performed.

In step 6, moments of the distribution are calculated from the contours.

$$n^* = 2\pi\,(\Delta v)^2\,\Sigma(f^* v_\perp), \tag{A8}$$

where Δv is the bin size in $v_\parallel$-$v_\perp$ space.

$$u_\parallel^* = \Sigma(u_\parallel f^*\, v_\perp) / \Sigma(f^* v_\perp), \tag{A9}$$

$$T_\parallel^* = (m/k)\,\Sigma(\,(v_\parallel - \langle v_\parallel\rangle)^2 f^* v_\perp) / \Sigma(f^* v_\perp), \tag{A10}$$

$$T_\perp^* = (m/2k)\,\Sigma(v_\perp^{\,3} f^*) / \Sigma(f^* v_\perp). \tag{A11}$$

In step 7, new values of the speed in the spacecraft coordinate system are then computed from the individual f_i calculated from (A7).

$$\langle u_x\rangle = \Sigma\, u_x f_i\, d^3{}_i v / \Sigma f_i\, d^3{}_i v, \tag{A12}$$

where the summations are over all subpixels of all pixels. Similar summations are used to find new values of $\langle u_y\rangle$ and $\langle u_z\rangle$.

In step 8, the value of $\langle \boldsymbol{u}\rangle$ calculated in step 7 is used to convert from the spacecraft to the plasma rest frame, and the process starts over again at step 3b.

Several subjective choices are required in implementing this algorithm. The first choice is the number of subpixels per pixel. We chose a square array because the θ and φ fields of view of the instrument are approximately equal. Division into 8×8 subpixels provides a velocity resolution close to the bin size in $v_\parallel$-$v_\perp$ space.

A more important choice is how far into the noise to carry the summations in the calculations of the moments. This has always been a problem in calculating temperatures from plasma spectra and is a principal source of discrepancies in temperature values reported by different people using different instruments. It is of special concern in the present situation because, in order to calculate contours of the logarithm of $\langle f(v)\rangle$, we do not allow zero or negative values of $\langle f(v)\rangle$ in any bin. Thus our background is slightly higher than the true background. There is not a single correct choice. We have limited the data used in our analysis in two steps. (1) At the start of the analysis of an ion spectrum, the data are sorted into proton pixels versus alpha-particle pixels on the basis of a 1-D spectrum formed by summing the distribution over all angles. Then, still working with the original pixels (before dividing into subpixels) for each type of ion separately, $v_\parallel$-$v_\perp$ space is divided into concentric shells about the origin, each shell having a radial thickness of Δv (the size of the bins). Starting outward from the seventh shell, we find the innermost shell for which at least one bin has data (i.e., at least one pixel falls in the shell) and for which (a) the total number of counts, summed over all pixels is <6 or (b) the average number of counts/pixel is <0.5. All pixels in and beyond that shell, whose inner radius is denoted by R_1, are dropped from further consideration. (2) In each iteration, we find a shell radius R_2 for which the average value of f^* in the shell just outside R_2 exceeds 1.5 times the average value of f^* in the shell just inside R_2. The calculation of the moments is limited to the region for which $R = \sqrt{(v_\parallel^2 + v_\perp^2)}$ is less than both R_1 and R_2. The requirement for the second cutoff R_2 arises from the occasional localized pileup of noise counts at large R which grows with each iteration until a local maximum may develop somewhere on the outer fringe of the distribution. Some evidence of this phenomenon can be seen at $(v_\parallel, v_\perp) \approx (135, 0)$ km/s in the bottom distribution in Figure 4.

Finally, there is the choice of the number of iterations to carry out. We are still experimenting with different algorithms, which may ultimately differ for protons and alphas and vary with solar distance. For the spectra used in the analysis for this paper, we generally carried out three iterations for both protons and alphas. This decision was made on the basis of several quality parameters. The first parameter, Q_g, tests the compliance of the iterated result with

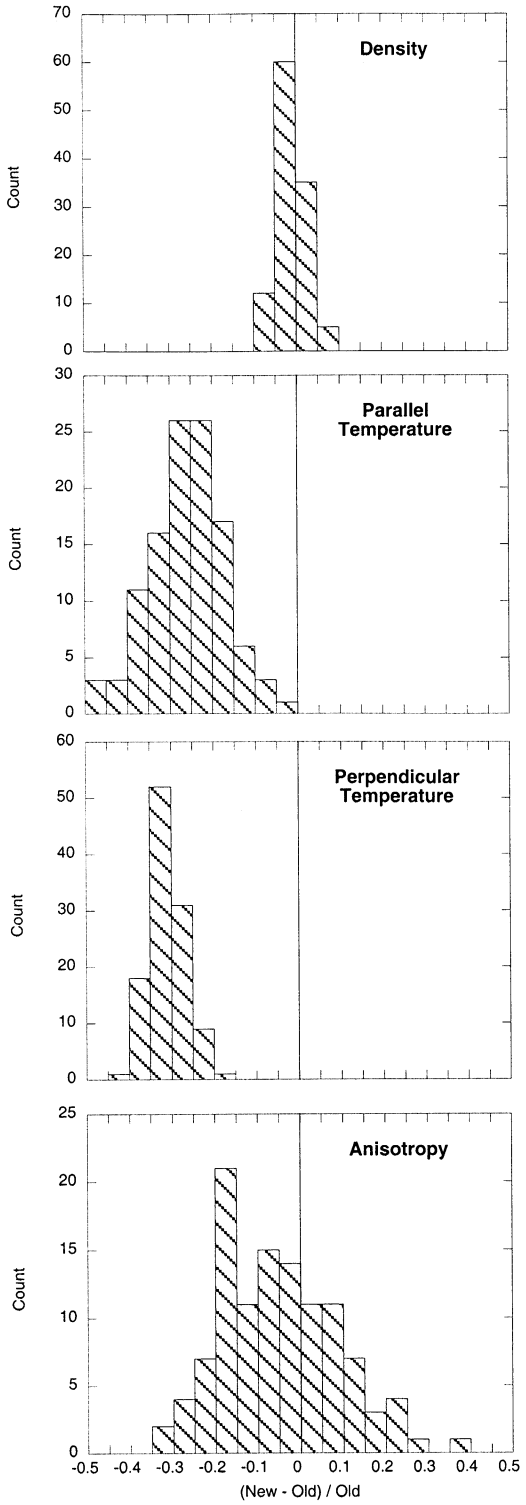

Figure A2. Distributions of the relative changes in plasma parameters resulting from the deconvolution process for the 12 hours of proton data used in this paper. For a parameter x the histograms show the distribution of the ratio $(x_{new} - x_{old})/x_{old}$.

the assumption of gyrotropy. Q_g is the average of the standard deviations of the values of f_i within each bin for which $<f(v)>$ is within a factor of 100 of the spectral peak normalized by the average value for that bin. The value of $u_\parallel$* calculated from (A9) serves as another quality parameter. If the contours were a perfect fit to the data and in the limit of very narrow bins, $u_\parallel$* would be zero. We also considered the shell number N_s corresponding to the cutoff R_2. Other parameters examined were the fractional changes in n*, $T_\parallel$* and $T_\perp$* from one iteration to the next. We considered an iterated result to be acceptable if the following criteria were met:

$$Q_g \le 0.6 \quad \text{(A13a)}$$

$$u_\parallel{}^* \le 3 \text{ km/s} \quad \text{(A13b)}$$

$$\Delta n^*/n^* < 0.03 \quad \text{(A13c)}$$

$$\Delta T_\parallel{}^*/T_\parallel{}^* < 0.05 \quad \text{(A13d)}$$

$$\Delta T_\perp{}^*/T_\perp{}^* < 0.05 \quad \text{(A13e)}$$

$$N_s \ge 20 \text{ protons}, \quad \ge 15 \text{ alphas} \quad \text{(A13f)}$$

where Δ indicates the absolute value of the change between successive iterations. For a majority of the spectra processed for this paper, the parameters Q_g and $u_\parallel$* passed through minima at the second or third iteration and then increased with further iteration. Examination of contour plots for different numbers of iterations revealed that the principal differences occurred at the fringes of the distributions close to background.

For the 12 hours of proton data processed for this paper, the success rate (i.e., the fraction of the spectra that met all the criteria in (A13) by the third iteration) was 0.85. The success rate declines with increasing distance from the Sun as the distributions become narrower and the count rates approach the instrument background.

The histograms in Figure A2 show the relative changes in the proton density, parallel and perpendicular temperatures, and anisotropy resulting from the deconvolution process. The changes in velocity were negligible, and the changes in density were small (<10%). As expected, both the parallel and perpendicular temperatures decreased while the anisotropy changed significantly in either direction.

In conclusion, we believe the deconvolution method outlined here is both successful and necessary to obtain realistic plasma parameters from the measured spectra.

Acknowledgments. We thank Bruce Tsurutani and Bimla Buti for helpful and provocative discussions about the interpretation of the results presented in this paper. We also thank Regina Sakurai for help with the contouring procedures described in the appendix. This work is the result of research performed at the Jet Propulsion Laboratory of the California Institute of Technology under a contract with the National Aeronautics and Space Administration.

Janet G. Luhmann thanks Thomas H. Zurbuchen and Naiguo Lin for their assistance in evaluating this paper

References

Balogh, A., T. J. Beek, R. J. Forsyth, P. C. Hedgecock, R. J. Marquedant, E. J. Smith, D. J. Southwood, and B. T. Tsurutani, The magnetic field investigation on the Ulysses mission: Instrumentation and preliminary scientific results, *Astron. Astrophys. Suppl., 92*, 221, 1992.

Bame, S. J., D. J. McComas, B. L. Barraclough, J. L. Phillips, K. J. Sofaly, J. C. Chavez, B. E. Goldstein, and R. K. Sakurai, The Ulysses solar wind plasma experiment, *Astron. Astrophys. Suppl., 92*, 237, 1992.

Baumgärtel, K., Soliton approach to magnetic holes, *J. Geophys. Res., 104*, 28,295, 1999.

Burlaga, L. F., Micro-scale structures in the interplanetary medium, *Sol. Phys., 4*, 67, 1968.

Chisham, G., S. J. Schwartz, D. Burgess, S. D. Bale, M. W. Dunlop, and C. T. Russell, Multisatellite observations of large magnetic depressions in the solar wind, *J. Geophys. Res., 105*, 2325, 2000.

Daughton, W., S. P. Gary, and D. Winske, Electromagnetic proton/proton instabilities in the solar wind: Simulations, *J. Geophys. Res., 104*, 4657, 1999.

Feldman, W. C., and E. Marsch, Kinetic phenomena in the solar wind, in *Cosmic Winds and the Heliosphere*, edited by J. R. Jokipii, C. P. Sonett, and M. S. Giampapa, p. 617, Univ. Ariz. Press, Tucson, 1997.

Feldman, W. C., B. L. Barraclough, J. L. Phillips, and Y.-M. Wang, Constraints on high-speed solar wind structure near its coronal base: A Ulysses perspective, *Astron. Astrophys., 316*, 355, 1996.

Fränz, M., D. Burgess, and T. S. Horbury, Magnetic field depressions in the solar wind, *J. Geophys. Res., 105*, 12,725, 2000.

Gary, S. P., S. A. Fuselier, and B. J. Anderson, Ion anisotropy instabilities in the magnetosheath, *J. Geophys. Res., 98*, 1481, 1993.

Gary, S. P., L. Yin, D. Winske, and D. B. Reisenfeld, Electromagnetic alpha/proton instabilities in the solar wind, *Geophys. Res. Lett., 27*, 1355, 2000.

Gloeckler, G., and J. Geiss, Interstellar and inner source pickup ions observed with SWICS on Ulysses, *Space Sci. Rev., 86*, 127, 1998.

Goldstein, B. E., M. Neugebauer, L. D. Zhang, and S. P. Gary, Observed constraint on proton-proton relative velocities in the solar wind, *Geophys. Res. Lett., 27*, 53, 2000.

Ho, C. M., B. T. Tsurutani, R. Sakurai, B. E. Goldstein, A. Balogh, and J. L. Phillips, Interplanetary discontinuities in corotating streams and their interaction regions, *Astron. Astrophys., 316*, 346, 1996.

Lepping, R. P., and K. W. Behannon, Magnetic field directional discontinuities, 1, Minimum variance errors, *J. Geophys. Res., 85*, 4695, 1980.

Lin, N., P. J. Kellogg, R. J. MacDowall, A. Balogh, R. J. Forsyth, J. L. Phillips, A. Buttighoffer, and M. Pick, Observation of plasma waves in magnetic holes, *Geophys. Res. Lett., 22*, 3417, 1995.

Lin, N., P. J. Kellogg, R. J. MacDowall, B. T. Tsurutani, and C. M. Ho, Langmuir waves associated with discontinuities in the solar wind: A statistical study, *Astron. Astrophys., 316*, 425, 1996.

MacDowall, R. J., N. Lin, P. J. Kellogg, A. Balogh, R. J. Forsyth, and M. Neugebauer, Langmuir waves in magnetic holes: Source mechanism and consequesces, in *Solar Wind Eight, AIP Conf. Proc 382*, edited by D. Winterhalter, J. T. Gosling, S. R. Habbal, W. S. Kurth, and M. Neugebauer, p. 301, Am. Inst. Physics, Woodbury, N. Y., 1996.

McComas, D. J., B. L. Barraclough, H. O. Funsten, J. T. Gosling, E. Santiago-Muñoz, R. M. Skoug, B. E. Goldstein, M. Neugebauer, P. Riley, and A. Balogh, Solar wind observations over Ulysses first full polar orbit, *J. Geophys. Res., 105*, 10,419, 2000.

McKean, M. E., D. Winske, and S. P. Gary, Two-dimensional simulations of ion anisotropy instabilities in the magnetosheath, *J. Geophys. Res., 99*, 11,141, 1994.

Neugebauer, M., D. R. Clay, B. E. Goldstein, B. T. Tsurutani, and R. D. Zwickl, A reexamination of rotational and tangential discontinuities in the solar wind, *J. Geophys. Res., 89*, 5395, 1984.

Neugebauer, M., B. E. Goldstein, E. J. Smith, and W. C. Feldman, Ulysses observations of differential alpha-proton streaming in the solar wind, *J. Geophys. Res., 101*, 17, 1996.

Reisenfeld, D. B., S. P. Gary, J. T. Gosling, D. J. McComas, J. T. Steinberg, B. E. Goldstein, and M. Neugebauer, Helium energetics in the high-latitude solar wind: Ulysses observations, *J. Geophys. Res., in press*, 2000.

Smith, E. J., Identification of interplanetary tangential and rotational discontinuities, *J. Geophys. Res., 78*, 2054, 1973.

Sonnerup, B. U. O., and L. J. Cahill, Jr., Magnetopause structure and altitude from Explorer 12 observations, *J. Geophys. Res., 72*, 171, 1967.

Stone, R. G., et al., The unified radio and plasma wave investigation on Ulysses, *Astron. Astrophys. Suppl., 92*, 291, 1992.

Tsurutani, B. T., and C. M. Ho, A review of discontinuities and Alfvén waves in interplanetary space: Ulysses results, *Rev. Geophys., 37*, 517, 1999.

Tsurutani, B. T., E. J. Smith, D. J. Southwood, and A. Balogh, Nonlinear magnetosonic waves and mirror mode structures in the March 1991 Ulysses interplanetary event, *Geophys. Res. Lett., 19*, 1267, 1992.

Tsurutani, B. T., G. S. Lakhina, D. Winterhalter, J. K. Arballo, C. Galvan, and R. Sakurai, Energetic particle cross-field diffusion: Interaction with magnetic decreases, *Nonlinear Processes Geophys., 6*, 235, 1999.

Turner, J. M., L. F. Burlaga, N. F. Ness, and J. F. Lemaire, Magnetic holes in the solar wind, *J. Geophys. Res., 82*, 1921, 1977.

Winterhalter, D., M. Neugebauer, B. E. Goldstein, E. J. Smith, S. J. Bame, and A. Balogh, Ulysses field and plasma observations of magnetic holes in the solar wind and their relation to mirror-mode structures, *J. Geophys. Res., 99*, 23,371, 1994.

Winterhalter, D., E. J. Smith, M. Neugebauer, B. E. Goldstein, and B. T. Tsurutani, The latitudinal distribution of solar wind magnetic holes, *Geophys. Res. Lett., 27*, 1615, 2000.

Zurbuchen, T. H., S. Hefti, L. A. Fisk, G. Gloeckler, N. A. Schwadron, C. W. Smith, N. F. Ness, R. M. Skoug, D. J. McComas, and L. F. Burlaga, On the origin of microscale magnetic holes, *J. Geophys. Res.*, in press, 2000.

S. P. Gary, Los Alamos National Laboratory, Los Alamos, NM 87545.

B. E. Goldstein, M. Neugebauer, E. J. Smith, and D. Winterhalter, MS 169-506, Jet Propulsion Laboratory, California Institute of Technology, Pasadena, CA 91109 (mneugeb@jplsp2.jpl.nasa.gov.).

R. J. MacDowall, NASA Goddard Space Flight Center, Greenbelt, MD 20771.

(Received August 29, 2000; revised October 24, 2000; accepted November 14, 2000.)